Journal of Materials Chemistry A

Accepted Manuscript

This article can be cited before page numbers have been issued, to do this please use: J. Kang, J. Jang, W. Koo, J. Seo, Y. Choi, M. Kim, D. Kim, H. Cho, W. Jung and I. Kim, *J. Mater. Chem. A*, 2018, DOI: 10.1039/C8TA02725K.

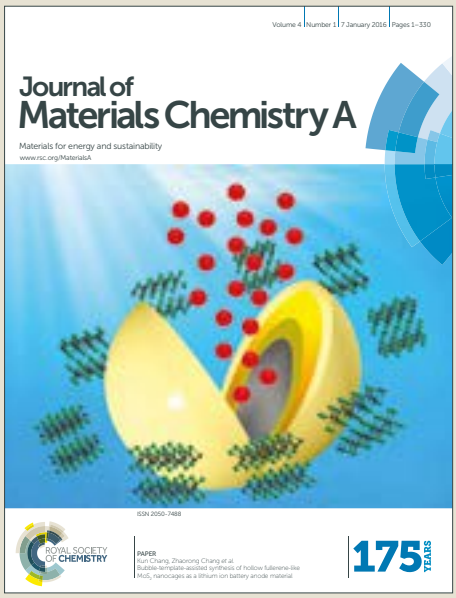

ROYAL SOCIETY OF CHEMISTRY

rsc.li/materials-a

View Article Online
DOI: 10.1039/C8TA02725K

Journal of Materials Chemistry A

ARTICLE

Perovskite $La_{0.75}Sr_{0.25}Cr_{0.5}Mn_{0.5}O_{3-\delta}$ Sensitized SnO_2 Fiber-in-Tube Scaffold: Highly Selective and Sensitive Formaldehyde Sensing

Received 00th January 20xx,
Accepted 00th January 20xx

DOI: 10.1039/x0xx00000x

www.rsc.org/

Joon-Young Kang, Ji–Soo Jang, Won-Tae Koo, Jongsu Seo, Yoonseok Choi, Min-Hyeok Kim, Dong-Ha Kim, Hee-Jin Cho, WooChul Jung and Il–Doo Kim*

In this work, highly porous SnO_2 fiber-in-tubes (FITs), which are functionalized with perovskite $La_{0.75}Sr_{0.25}Cr_{0.5}Mn_{0.5}O_{3-\delta}$ (LSCM) particles as chemical sensitizer, are used as a superior formaldehyde (CH_2O) sensing layer. LSCM-loaded as-spun Sn precursor/polymer composite fibers are rapidly calcined to create porous fiber-in-tube (FIT) SnO_2 structure with high surface area. Such unique morphological evolution originates from Ostwald ripening effect and crystal growth inhibition caused by LSCM particles. Furthermore, LSCM particles with high oxygen vacancies concentration and a large work function significantly promote oxygen spillover and electron depletion on the surface of SnO_2 (6.80 eV for LSCM vs. 4.55 eV for SnO_2). As a result, LSCM-loaded SnO_2 FITs (LSCM@SnO_2 FITs) provide remarkably high response to formaldehyde (R_{air}/R_{gas} = 26.50 to 5 ppm) and excellent selectivity against interfering gases (H_2S, C_7H_8, NH_3, C_2H_6O, C_8H_{10}, CO, and C_5H_{12}) even without using noble metal catalysts. These observations demonstrate the potential use of LSCM@SnO_2 FITs for real-time monitoring of indoor air quality, especially toward formaldehyde, which has not been accurately detected by conventional metal oxide based sensors.

Introduction

Recently, detection of various toxic chemical gas species has emerged as a critical issue owing to their potential dangers posed to human body as well as the environment.[1] For instance, toluene (C_7H_8), xylene (C_8H_{10}), and formaldehyde (CH_2O) are major causes of sick building syndrome, which is a medical symptom that develops in people suffering from poor indoor air quality.[2,3] In particular, inhalation of parts per million (ppm) level of formaldehyde in short time can cause significant health problems such as nausea (0.2–1.9 ppm), lachrymation (4–20 ppm), pulmonary edema (30–50 ppm), and even death (>50 ppm).[4, 5] Besides, since the sub-ppm levels of toxic vapors are odorless or colorless, it is difficult for a person to notice exposure to such gases. In this sense, sensitive and selective detection toward formaldehyde, particularly at sub-ppm concentration is highly required for accurate monitoring of indoor air quality.

Among various chemical gas sensing materials, semiconducting metal oxides (SMOs) have been commonly utilized due to their facile synthesis process, easy miniaturization, and low fabrication cost.[6, 7] In particular, given that the reaction between SMOs and target analytes occurs on the surface of SMOs, one-dimensional (1D) nanostructures with large surface area and high porosity are considered as one of the most ideal sensing layers.[8] Among various synthetic routes for 1D structures, electrospinning has unique advantages due to easy tuning of composition and morphological tailoring including nanofibers (NFs),[9] nanotubes (NTs),[10] and fiber-in-tubes (FITs).[11] In particular, the FIT nanostructures with voids between core fiber and thin shell can enlarge surface area as compared with the solid NFs or hollow NTs structures, facilitating gas diffusion onto porous sensing layers. Although FIT structures have been explored for energy storage materials,[11, 12] these unique structures have been rarely employed as chemiresistive gas sensing layers.

In addition to the facile synthesis of SMOs nanostructures with high porosity and enhanced surface area, their catalytic functionalization is essential to further enhance sensitivity and selectivity toward interfering gases. So far, noble metal catalysts such as Pt, Pd, and Rh have been widely studied to effectively promote the gas sensing properties of SMOs by means of electronic and/or chemical sensitization.[8, 13] However, scarcity of noble metals, their high costs, and sensor-to-sensor variation in performance due to the poisoning of these catalysts hinder their practical use in commercialized gas sensors. Moreover, nanoscale catalysts readily agglomerate and degrade after long operation cycles particularly at high operating temperature.[14] Therefore, a new catalytic material with outstanding thermal stability and low cost is highly desired for SMOs-based chemiresistors.

Perovskite oxides (ABO_3) have been extensively studied as stable oxide catalysts in diverse applications including electrochemical oxidation/reduction in solid oxide fuel cell,[15]

*Department of Materials Science and Engineering, Korea Advanced Institute of Science and Technology (KAIST), 291 Daehak-ro, Yuseong-gu, Daejeon 34141, Republic of Korea. *E-mail: idkim@kaist.ac.kr*

‡Electronic Supplementary Information (ESI) available. See DOI: 10.1039/x0xx00000x

View Article Online
DOI: 10.1039/C8TA02725K

Li-air cell,[16] and hydrocarbon oxidation in catalytic converters[17] due to their excellent thermal stability, low cost, tunable electrical and redox properties by facile substitution of cations.[18] Especially, some perovskite oxides such as $LaCoO_3$ and $LaMnO_3$ are known to possess outstanding oxygen storage capability, *i.e.*, oxygen adsorption/desorption properties, which are ascribed to the generation of abundant oxygen vacancies within ABO_3 lattice.[19] For instance, oxygen species in lanthanum-based perovskite desorb in certain ranges of temperature; desorption of oxygen species adsorbed on oxygen vacancies (O^-) at 300–700 °C and lattice oxygen (O^{2-}) at temperatures higher than 700 °C.[20] Since SMOs-based gas sensors are usually operated in the range of 200–500 °C,[21] perovskite oxides with suitable composition may supply sufficient oxygen molecules to SMOs when they are decorated on the surface of SMOs. It is important to note that oxygen species chemisorbed on the surface of the sensing layers serve as reaction sites for target analytes, the reaction of which leads to electrical resistance variation. Recently, Lin et al. have reported $La_{0.8}Sr_{0.2}FeO_3$ (LSFO) sensitized Ga_2O_3 nanorods for detection of carbon monoxide.[22] Although the sensing characteristics of Ga_2O_3 nanorods were 8.75-fold improved, the catalytic role of perovskite oxides at high temperature has been rarely investigated, particularly in terms of their oxygen supplying effect.

In this work, we investigate the catalytic role of perovskite oxide particles functionalized on SnO_2 fiber-in-tube architectures as superior formaldehyde sensing layers. Here, $La_{0.75}Sr_{0.25}Cr_{0.5}Mn_{0.5}O_{3-\delta}$ (LSCM) particles are selected as an efficient oxygen suppliers, where Sr and Mn cations are substituted in A- and B- sites. A solution (Sn precursor/matrix polymer) containing dispersed LSCM particles is electrospun to form LSCM embedded Sn precursor/polymer composite NFs. During the subsequent calcination, discretely decorated LSCM particles effectively hinder the outward diffusion of Sn ions, resulting in generation of fibrous core in the tubular structure, *i.e.*, LSCM-loaded SnO_2 FITs (hearafter, LSCM@SnO_2 FITs). The unique catalytic role of LSCM particles decorated on SnO_2 FITs and their sensitive and selective formaldehyde detection characteristics are discussed in comparison with pristine SnO_2 NTs and $LaCrO_3$-decorated SnO_2 FITs as control samples.

Experimental section

Materials

Polyvinylpyrrolidone (PVP, M_w = 1,300,000 g mol^{-1}), tin(II) chloride dihydrate ($SnCl_2{\cdot}2H_2O$, 99.995%), lanthanum(III) nitrate hexahydrate ($La(NO_3)_3{\cdot}6H_2O$, 99.99%), strontium nitrate ($Sr(NO_3)_2$, 99.0%), chromium(III) nitrate nonahydrate ($Cr(NO_3)_3{\cdot}9H_2O$, 99%), manganese(II) nitrate tetrahydrate ($Mn(NO_3)_2{\cdot}4H_2O$, 97.0%), ethanol (EtOH, 99.5%), citric acid ($C_6H_8O_7$, 99%), ethylene glycol ($(CH_2OH)_2$, 99.8%) and *N,N*-dimethylformamide (DMF, 99.8%) were purchased from Sigma-Aldrich (St. Louis, USA). Lanthanum chromite particles ($LaCrO_3$, 99.5%) were purchased from Alfa Aesar. All chemicals were used without further purification.

Synthesis of LSCM particles

LSCM particles were synthesized by combustion method using citric acid, as reported elsewhere.[23] Briefly, 0.75 mmol of $La(NO_3)_3{\cdot}6H_2O$ (0.243 g), 0.25 mmol of $Sr(NO_3)_2$ (0.053 g), 0.5 mmol $Cr(NO_3)_3{\cdot}9H_2O$ (0.200 g), 0.5 mmol $Mn(NO_3)_2{\cdot}4H_2O$ (0.126 g) and 1 ml of ethylene glycol was added in 3 ml of deionized water (DIW). Then, 4 mmol of citric acid (0.768 g) was added to the nitrate precursors dissolved solution. After vigorous stirring at 70 °C, the precipitated gel was dried for overnight, and then heated at 350 °C for 1 h. Then the obtained powders were heated in ambient condition at 1100 °C for 8 h. As a result, LSCM particles with an average diameter of 215 nm were obtained.

Synthesis of LSCM@SnO_2 FITs, LCO@SnO_2 FITs, and SnO_2 NTs

To prepare the electrospinning solution, 0.25 g $SnCl_2{\cdot}2H_2O$ and 0.35 g of PVP were dissolved in 2.7 g of co-solvent consisting of 1.35 g of DMF and 1.35 g of ethanol and vigorously stirred at 300 rpm at room temperature for 5 h. Then, the different amounts of LSCM particles (4.18, 8.35, 16.7, and 25.1 mg, for 2.5, 5, 10, and 15 wt% LSCM loaded SnO_2 FITs, respectively) were added to the electrospinning solution and stirred at 60 °C for 8 h with stirring speed of 300 rpm. After stirring, LSCM particles were dispersed in the solution. The electrospinning solution was sonicated for 2 h in an ultrasonic bath to fully disperse LSCM particles and dissolve the metal precursors and PVP in the solution. After stirring and sonication step, LSCM particles were homogeneously dispersed in the electrospinning solution. Afterwards, electrospinning was carried out with the prepared solution at a constant voltage of 13 kV applied between the stainless collector and the metal syringe needle of 21 gauge. The feeding rate was set at 0.1 ml·min^{-1} while the distance between the collector and needle was maintained at 15 cm. The as-spun NFs were collected on the stainless steel collector. As-spun NFs were transformed into LSCM@SnO_2 FITs upon heat treatment at 600 °C in air. To fabricate nanotubular structures, fast ramping rate of 10 °C·min^{-1} was maintained during the calcination step. $LaCrO_3$-functionalized SnO_2 FITs (LCO@SnO_2 FITs) were prepared by the same experimental procedures, except that LCO particles were used instead of LSCM particles. In addition, pristine SnO_2 NTs were fabricated through the same experimental procedure without using LSCM particles.

Synthesis of LSCM@SnO_2 NFs and SnO_2 NFs

As-spun NFs were obtained by the same experimental procedure as LSCM@SnO_2 FITs. To fabricate densely packed fibers, a moderate ramping rate of 5 °C·min^{-1} was maintained during the calcination of the as-spun NFs in air. Pristine SnO_2 NFs were fabricated through the same experimental process without using LSCM particles.

Evaluation of gas sensing performance

To measure the gas sensing characteristics, we fabricated gas sensors on Al_2O_3 substrates (area: 2.5 mm x 2.5 mm, thickness: 0.2 mm). The substrates are patterned with two parallel Au electrodes on the front side and Pt heater on the back side. 6 mg

View Article Online
DOI: 10.1039/C8TA02725K

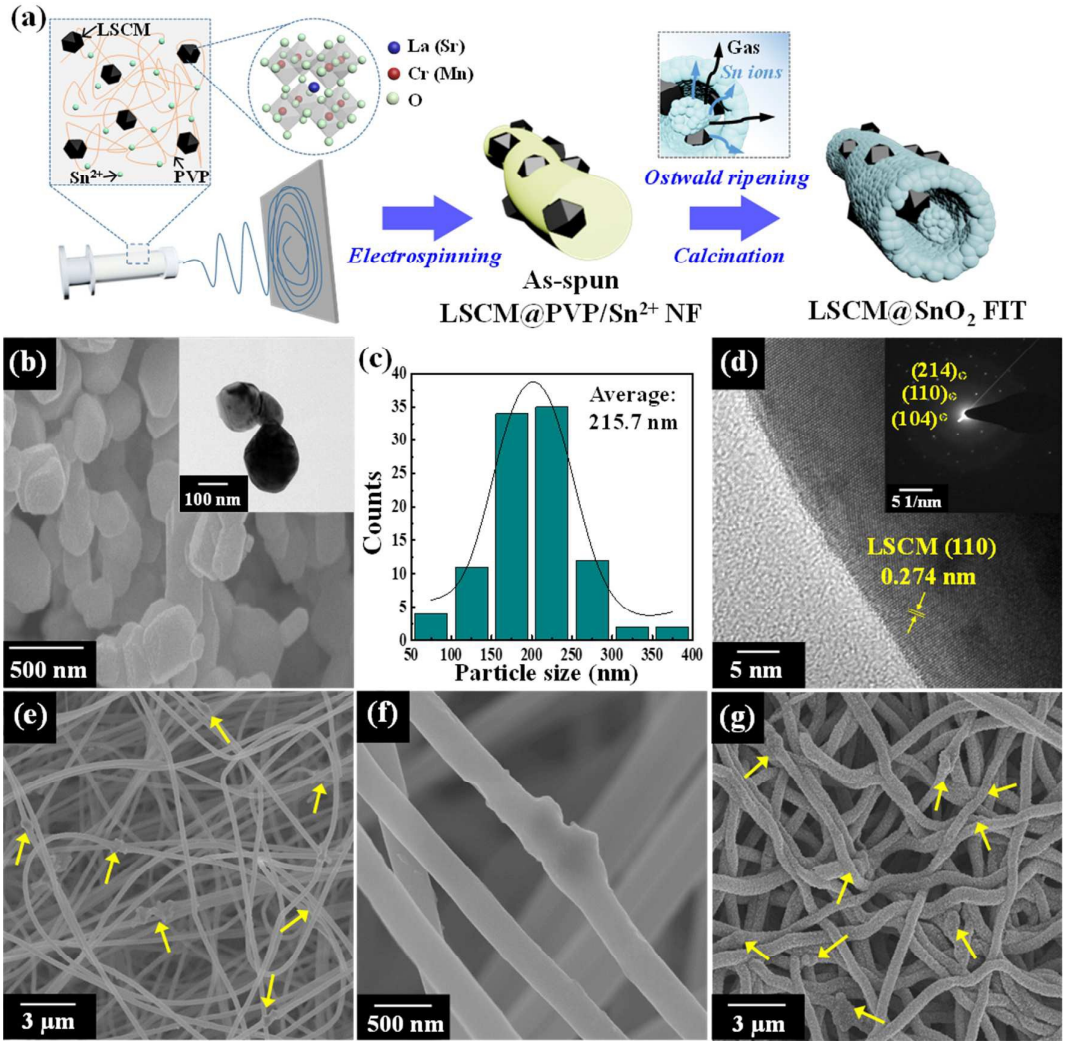

Fig. 1 a) Schematic illustration of the experimental procedure. b) SEM image of LSCM particles with TEM image of LSCM in the inset. c) Size distribution of LSCM particles. d) HRTEM image of LSCM particles with SAED pattern of LSCM particles in the inset. e) SEM image of LSCM@PVP/Sn NFs. f) Magnified SEM image of LSCM@PVP/Sn NFs. g) SEM image of LSCM@SnO_2 FITs.

of prepared sensing materials (LSCM@SnO_2 FITs, LCO@SnO_2 FITs and SnO_2 NTs) were dispersed in 300 µL of EtOH. Then, the dispersed solutions for each sensing material were drop-coated on the substrates. All the sensors were stabilized in ambient condition for 3 h before sensing tests. To investigate the sensitivity to target gas, the sensors were exposed to 8 kinds of gas species (formaldehyde, hydrogen disulfide, toluene, ammonia, ethanol, p-xylene, carbon monoxide, and pentane). The gases were injected for 10 minutes at each concentration in the range of 1-5 ppm with 10 min interval of air injection. We measured the resistance changes of each sensor by using data acquisition system (34972A, Agilent), and the obtained data were translated into gas response, *i.e.*, R_{air}/R_{gas}, where R_{air} is the baseline resistance in air and R_{gas} is the resistance in gas. The response time of the sensor was calculated as the time to decrease the resistance by 90% of the difference ($R_{air} - R_{gas}$). The operating temperature was controlled by applying a voltage to the Pt microheater using a DC power supply (E3647A, Agilent). The principal component analysis (PCA) was conducted by using IBM SPSS software.

Characterization

To investigate the microstructures and morphologies of the prepared samples, field emission scanning electron microscopy (Nova230, FEI) and field emission transmission electron microscopy (Tecnai, G2 F30 S-Twin, FEI) were used. Powder X-ray diffraction (D/MAX-2500, Rigaku) with Cu Kα radiation (λ = 1.5418 Å) was conducted to confirm the crystal structure of the samples. X-ray photoelectron spectroscopy (K-alpha, Thermo VG Scientific) using Al Kα radiation was used to investigate the chemical binding states. Ultraviolet photoelectron spectroscopy (UPS) (Sigma Probe, Thermo VG

View Article Online
DOI: 10.1039/C8TA02725K

Scientific) using He I source (21.22 eV) was conducted to investigate the work functions and valence band maxima of the samples. The pore size distribution and Brunauer-Emmett-Teller (BET) surface area of samples were confirmed by using N_2 adsorption/desorption isotherms (Tristar 3020, Micromeritics) at 77 K.

Results and Discussion

Fig. 1a shows schematic illustration of the experimental procedure. The synthesized LSCM particles exhibited quasi-spherical shapes (Fig. 1b), with an average size of 215.7 nm, as previously reported (Fig. 1c).[23] High resolution transmission electron microscopy (HRTEM) images and selected area electron diffraction (SAED) pattern revealed high crystallinity of LSCM particles, showing hexagonal crystal structure with (110) lattice and diffraction pattern from (104), (110), and (214) crystal planes (Fig. 1d). The LSCM particles were introduced in the electrospinning solution and vigorously stirred. Upon subsequent electrospinning, LSCM particles were homogeneously distributed on the as-spun Sn precursor/PVP NFs (Fig. 1e and f). The as-spun Sn precursor/PVP/LSCM composite NFs were transformed into 1D SnO_2 nanotubular structures during calcination at 600 °C in air (ramping rate of 10 °C min^{-1} from room temperature). LSCM particles were tightly immobilized on the 1D SnO_2 structures, inducing local bumpy surface morphologies (Fig. 1g). According to the previous studies, fast ramping rate during calcination of as-spun composite NFs results in the creation of tubular metal oxide (SnO_2) structures triggered by Ostwald ripening behavior of SnO_2, while moderate ramping rate (5 °C min^{-1}) forms densely packed SnO_2 NFs.[10] It was reported that co-solvents (DMF and highly volatile ethanol) used for synthesis of as-spun composite NFs triggered Ostwald ripening during rapid ramping step. However, in this work, fiber-in-tube structures are formed upon rapid calcination (10 °C min^{-1}) of 5 wt% LSCM loaded as-spun Sn precursor/PVP NFs (Fig. 2a). This morphological feature is attributed to the grain growth inhibition effect of LSCM particles that hinders Ostwald ripening

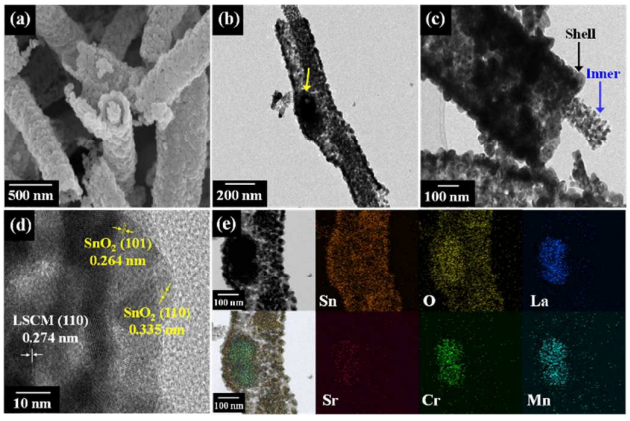

Fig. 2 a) Magnified SEM image of LSCM@SnO_2 FITs. b) TEM image of LSCM@SnO_2 FITs. c) Magnified TEM image of LSCM@SnO_2 FITs. d) HRTEM image of LSCM@SnO2 FITs. e) EDS mapping images of LSCM@SnO_2 FITs.

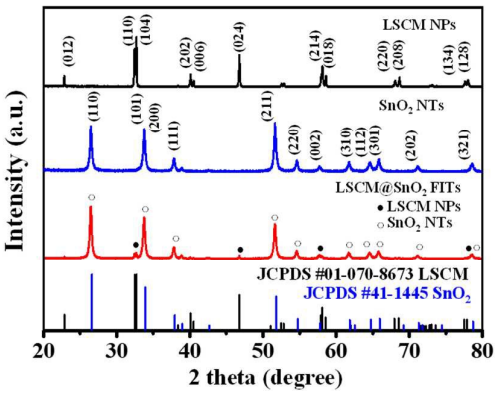

Fig. 3 XRD patterns of LSCM particles, pristine SnO_2 NTs, and LSCM@SnO_2 FITs.

of SnO_2 during the ramping step.

As Wu et al. demonstrated previously, during calcination the as-spun NFs undergo nanostructural evolution from dense fibers to tubes including core fibril structure, *i.e.*, FITs, as intermediate structures.[24] In our case, sub-micron sized LSCM particles affect inward diffusion of oxygen and outward diffusion of volatile byproducts and Sn ions during the ramping stage, thus hindering their escape from core of the NFs. Consequently, the unique FIT structures were formed. For comparison, we synthesized pristine SnO_2 NTs under the same experimental procedures without adding LSCM particles. As shown in Figure S1a, no fibrous SnO_2 were formed in the core of the NTs. Interestingly, loading amounts of LSCM particles affect morphological evolution of 1D SnO_2 structures. The interior fibers with smaller diameter (~80 nm) were formed in case of 2.5 wt% LSCM-loaded SnO_2 FITs compared to interior fiber diameter (~ 130 nm) of 5 wt% LSCM loaded SnO_2 FITs (Fig. S1b). On the other hand, the tubular structure was not observed in the case of 30 wt% LSCM-loaded SnO_2 because the excessive amount LSCM particles impeded the outward diffusion of Sn ions during calcination (Fig. S1c). To investigate the microstructures of LSCM@SnO_2 FITs in detail, transmission electron microscopy (TEM) analysis was conducted. The fiber-in-tube structure functionalized with LSCM particles was clearly identified (Fig. 2b). The fact that the grain sizes of the interior SnO_2 (~10 nm) are smaller compared to that (~40 nm) of SnO_2 comprising the shell indicates that crystallization of the shell was significantly influenced by Ostwald ripening, whereas the interior SnO_2 was not affected due to the grain growth inhibition caused by LSCM particles (Fig. 2c). HRTEM image shows the crystal planes of SnO_2 (110) and (101), and LSCM (110), which correspond to the interplanar spacing of 3.35 Å, 2.64 Å, and 2.74 Å, respectively (Fig. 2d).[10] In addition, SAED patterns exhibit the SnO_2 crystal plane of (110), (101), and (211) (Fig. S2). However, the other crystal planes of LSCM were not clearly identified because they mostly remained inside the SnO_2 tubes. To further clearly confirm the existence of LSCM particles, energy dispersive X-ray spectroscopy (EDS) elemental mapping analysis was carried out (Fig. 2e). The EDS mapping images revealed that Sn and O were homogeneously distributed in the SnO_2 FIT structures. Similarly, La, Sr, Cr, and

View Article Online
DOI: 10.1039/C8TA02725K

Mn elements were also finely distributed in the two adjacent LSCM particles.

In order to investigate the crystal structures of LSCM particles, pristine SnO_2 NTs, and LSCM@SnO_2 FITs, we carried out X-ray diffraction (XRD) analysis (Fig. 3). The XRD results exhibited rhombohedral crystal structure of LSCM particles (JCPDS No. 01–070–8673), in agreement with SAED pattern (inset of Fig. 1d). The crystal planes of tetragonal SnO_2 (JCPDS No. 41–1445) were identified in both SnO_2 NTs and LSCM@SnO_2 FITs. Furthermore, the perovskite crystal planes of LSCM particles were observed in LSCM@SnO_2 FITs calcined at 600 °C due to the inherent high thermal stability of perovskite oxides.[20] We selected perovskite $LaCrO_3$ (hereafter, LCO) particles as a control sample to compare their catalytic effect with LSCM particles as oxygen suppliers to the sensing layer. Since LCO particles have high thermal stability,[25] their crystal planes (JCPDS No. 33–0701) were also maintained in calcined LCO@SnO_2 FITs (Fig. S3).

X-ray photoelectron spectroscopy (XPS) was carried out to verify the chemical bonding nature of each element (Fig. 4). The two distinct Sn 3*d* peaks assignable to Sn^{4+} were observed at 486.5 and 495.0 eV for $3d_{5/2}$ and $3d_{3/2}$, respectively (Fig. 4a),[9] indicating the formation of SnO_2. The asymmetric 1*s* peaks of oxygen revealed two chemical states corresponding to O^{2-} and O^- with binding energies of 530.3 and 531.1 eV,[26] which represent lattice oxygen and chemisorbed oxygen species, respectively (Fig. 4b). In the case of LSCM particles-loaded SnO_2 FITs, the 3*d* peaks of La^{3+} showed clear doublet split at 834.8 eV for $3d_{5/2}$ and 851.2 eV for $3d_{3/2}$,[27] owing to the charge transfer from the ligand 2*p* to the La 4*f* levels, with the gap of ~3.7 eV between doublets (Fig. 4c).[28] In the spectrum of Sr, two 3*d* peaks of Sr^{2+} were observed at 133.6 and 135.7 eV that correspond to the $3d_{5/2}$ and $3d_{3/2}$ peaks, respectively, in the vicinity of Sn^{4+} peak at 138.7 eV (Fig. 4d).[29] The chemical states of Cr were identified as Cr^{3+} and Cr^{6+}; 576.4 eV for $2p_{3/2}$ and 585.9 eV for $2p_{1/2}$ of Cr^{3+}, and 579.7 eV for $2p_{3/2}$ and 588.1 eV for $2p_{1/2}$ of Cr^{6+} (Fig. 4e).[27] Similarly, $2p_{1/2}$ and $2p_{3/2}$ peaks of Mn were deconvoluted into two peaks corresponding to Mn^{3+} and Mn^{4+} (Figure 4f). The 2*p* peaks of Mn were observed at 653.9 and 642.3 eV for $2p_{1/2}$ and $2p_{3/2}$ peaks, respectively. The peaks for $2p_{3/2}$ and $2p_{1/2}$ of Mn^{3+} were observed at 641.1 and 652.8 eV, while the $2p_{3/2}$ and $2p_{1/2}$ peaks for Mn^{4+} were observed at 642.6 and 654.9 eV, respectively.[30]

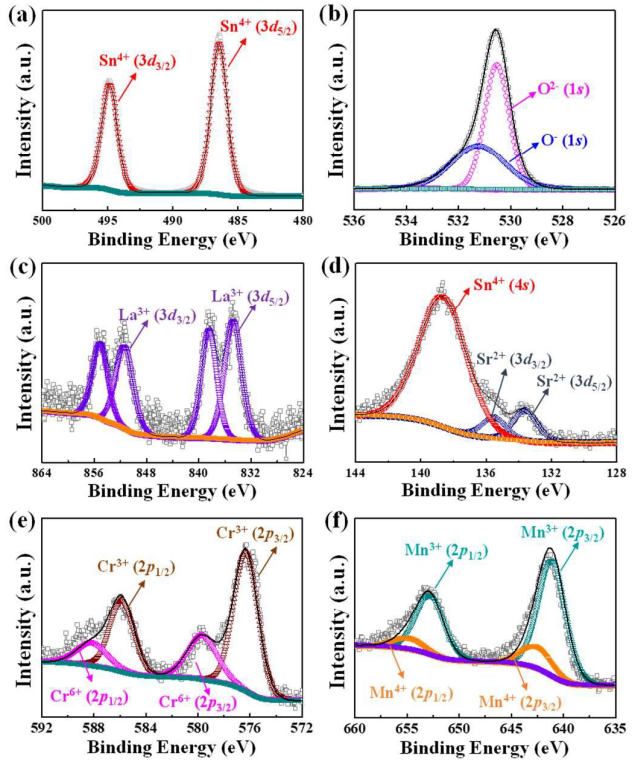

Fig. 4 High resolution XPS spectra of LSCM@SnO_2 FITs: a) Sn 4d. b) O 1s. c) La 3d. d) Sr 3d. e) Cr 2p. f) Mn 2p.

In order to investigate the catalytic effect of perovskite LSCM sensitizers and morphological effect of fiber-in-tube structures on sensing performances, we measured the formaldehyde sensing characteristics of 5 different samples, *i.e.*, pristine SnO_2 NFs, SnO_2 NTs, LCO@SnO_2 FITs, LSCM@SnO_2 NFs, and LSCM@SnO_2 FITs, using a homemade testing equipment.[31] $LaCrO_3$ particles with an average size of 200 nm are stoichiometric perovskite oxides without any substitution or doping, so they were used to compare the effect of substitution on the catalytic ability of LSCM particles (Fig. S4a). LCO@SnO_2 FITs were prepared in the same way as LSCM@SnO_2 FITs, while LSCM@SnO_2 NFs were achieved upon calcination of as-spun NFs at moderate ramping rate of 5 °C min^{-1} (Fig. S4b–d). The as-synthesized 1D sensing materials were dispersed in ethanol solution and sonicated to make a paste. Five sensors based on arrays of pristine SnO_2 NFs, SnO_2 NTs, LCO@SnO_2 FITs, LSCM@SnO_2 NFs, and LSCM@SnO_2 FITs were prepared by drop-coating the prepared paste on alumina substrates (more detail in the Experimental Section). We varied the loading amount of LSCM particles (pristine, 2.5, 5.0,

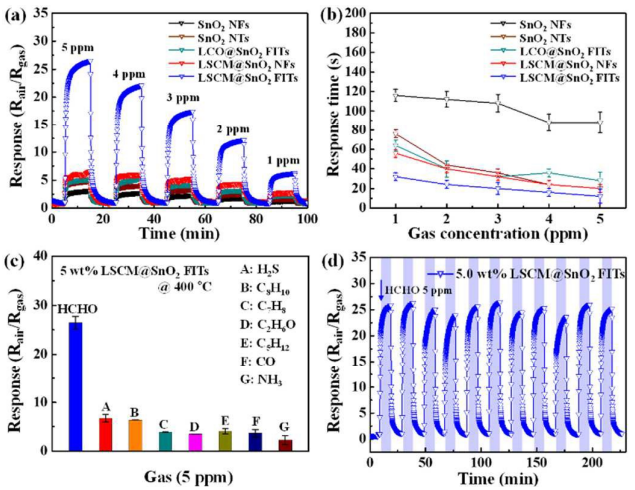

Fig. 5 a) Dynamic formaldehyde response transition of pristine SnO_2 NFs, SnO_2 NTs, 5 wt% LCO@SnO_2 FITs, 5 wt% LSCM@SnO_2 NFs and 5 wt% LSCM@SnO_2 FITs in the concentration range of 1–5 ppm at 400 °C. b) Response time in the concentration range of 1–5 ppm. c) Selectivity test of 5 wt% LSCM@SnO_2 FITs against 5 ppm of interfering analytes. d) Sensing property of 5 wt% LSCM@SnO_2 FITs under repeated exposure to 5 ppm of formaldehyde.

View Article Online
DOI: 10.1039/C8TA02725K

10, and 15 wt%) to investigate an optimum loading weight, considering that the excessive loading of the catalysts can lead to the significant degradation of sensing properties.[32] In addition, since the SMO based gas sensors exhibit temperature-dependent sensing characteristics,[21] we carefully examined the sensing temperature in the range of 350–500 °C. Considering the oxygen chemisorption temperature on the surface of SnO_2 (200–500 °C) and specific temperature range (300–700 °C) for oxygen desorptive property of perovskite, the sensing temperature should be optimized in high temperature range (350–500 °C). The sensing results indicated that 5 wt% LSCM@SnO_2 FITs exhibited the highest response toward 1–5 ppm of formaldehyde at 400 °C (Fig. S5). At same temperature, sensing properties of pristine SnO_2 NFs, SnO_2 NTs, 5 wt% LCO@SnO_2 FITs, 5 wt% LSCM@SnO_2 NFs, and 5 wt% LSCM@SnO_2 FITs toward formaldehyde were compared in the concentration range of 1–5 ppm (Fig. 5a). The LSCM@SnO_2 FITs showed the highest response to 5 ppm of formaldehyde (R_{air}/R_{gas} = 26.50), compared to that of LSCM@SnO_2 NFs (R_{air}/R_{gas} = 6.60), LCO@SnO_2 FITs (R_{air}/R_{gas} = 5.17), pristine SnO_2 NTs (R_{air}/R_{gas} = 4.85), and SnO_2 NFs (R_{air}/R_{gas} = 3.12). Moreover, LSCM@SnO_2 FITs exhibited highly improved response time (< 32 s) than that of LSCM@SnO_2 NFs (< 56 s), LCO@SnO_2 FITs (< 64 s), pristine SnO_2 NTs (< 76 s), and SnO_2 NFs (< 116 s) (Fig. 5b). The response times of sensors were calculated using R_{air} and R_{gas} values presented in Table S1. Detail calculation results of the response time were displayed in Fig. S6. In addition, LSCM@SnO_2 FITs and LSCM@SnO_2 NFs exhibited enhanced recovery speed (mean recovery time of 254.4 s and 231.2 s, respectively) compared to other control samples (Fig. S7). Furthermore, to investigate the selectivity of LSCM@SnO_2 FITs, sensing tests toward 5 ppm of various gas molecules, *i.e.*, formaldehyde (CH_2O), hydrogen disulfide (H_2S), p-xylene (C_8H_{10}), toluene (C_7H_8), ethanol (C_2H_6O), pentane (C_5H_{12}), carbon monoxide (CO), and ammonia (NH_3) were carried out at 400 °C (Fig. 5c). LSCM@SnO_2 FITs exhibited superior selectivity toward formaldehyde (R_{air}/R_{gas} = 26.50), while showing much lower responses (R_{air}/R_{gas} < 7) to interfering analytes. Moreover, LSCM@SnO_2 FITs showed excellent stability (R_{air}/R_{gas} = 25.38 ± 0.93) against 11 repeated sensing tests toward 5 ppm of formaldehyde at 400 °C (Fig. 5d). These results clearly revealed that the LSCM particles on SnO_2 FITs acted as effective sensitizers, particularly for the selective detection of formaldehyde gas.

The distinctive formaldehyde sensing characteristics of LSCM@SnO_2 FITs are attributed to three features, *i.e.*, (i) formation of heterojunction between SnO_2 and LSCM particles, (ii) catalytic effect of LSCM particles with abundant oxygen vacancy sites, and (iii) structural effects of FIT nanostructures (Fig. 6a). These effects can be interpreted as follows. The dynamic resistance variation graphs of SnO_2 NFs, SnO_2 NTs, LCO@SnO_2 FITs, LSCM@SnO_2 NFs, and LSCM@SnO_2 FITs were compared as shown in Fig. 6b. Basically, the sensing mechanism of SMOs involves the resistance variation by the surface reaction between chemisorbed oxygen and analyte gas

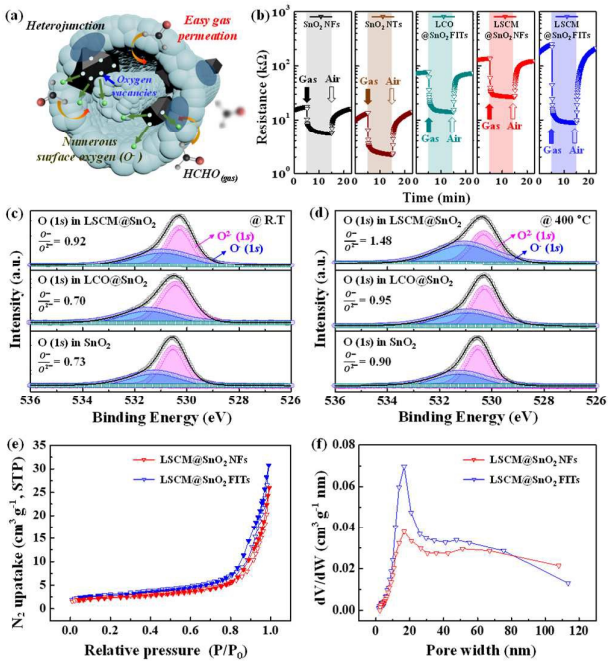

Fig. 6 a) Schematic illustration of formaldehyde sensing mechanism for LSCM@SnO_2 FITs. b) Dynamic resistance transition toward 5 ppm of formaldehyde at 400 °C. c) Ex-situ XPS spectra using high resolution scan mode of pristine SnO_2 NTs, 5 wt% LCO@SnO_2 FITs, and 5 wt% LSCM@SnO_2 FITs: O 1s at room temperature. d) O 1s after heating at 400 °C for 5 h in the sensing chamber. e) BET surface area, and f) pore size distribution of LSCM@SnO_2 FITs and LSCM@SnO_2 NFs.

molecules.[33] The width of depletion region of n-type SMOs becomes thinner when reducing gas molecules such as formaldehyde react with chemisorbed oxygen species and provide electrons to SMOs. Therefore, numerous sites for chemisorbed oxygen and large depletion region on the surface in air atmosphere can lead to the high response toward target gases. The results exhibited the increase in baseline resistance of LSCM@SnO_2 FITs (253.03 kΩ), compared to that of pristine SnO_2 NFs (17.86 kΩ) SnO_2 NTs (13.64 kΩ), LCO@SnO_2 FITs (78.42 kΩ), and LSCM@SnO_2 NFs (140.08 kΩ), which is attributed to the enlarged electron depletion region due to formation of a heterojunction between SnO_2 and LSCM (LCO) particles. Since the work function of SnO_2 (4.55 eV) is lower than that of LSCM particles (6.8 eV),[9] which was analyzed by ultraviolet photoelectron spectroscopy (UPS) (Fig. S8), the transition of electrons can be induced from SnO_2 to LSCM. Thus, huge electron depletion region formed on SnO_2 by the creation of heterojunction leads to the increased baseline resistance. Similarly, the increase in baseline resistance was also confirmed in LCO@SnO_2 FITs due to the heterojunction between SnO_2 and LCO (work function = 6.2 eV).[27] It is known that the substitution of Sr^{2+} in La-based perovskite increases work function of perovskite.[34] Therefore, the electron depletion region at the surface of SnO_2 can be further modulated by increased heterojunction effect. Accordingly, the smaller work function of LCO (6.2 eV) compared to that of LSCM (6.8 eV) induce lower Schottky barrier between the

View Article Online
DOI: 10.1039/C8TA02725K

Table 1. Spectra feature tables of oxygen 1s of LSCM@SnO2 FITs at after heating at 400 °C and room temperature.

Temperature	Element / Transition	Peak Area [eV counts]	Peak ratio [O^-/O^{2-}]
400 °C	O^{2-} (1s) in LSCM@SnO_2	96799.45	1.48
	O^- (1s) in LSCM@SnO_2	143634.74	
	O^{2-} (1s) in LCO@SnO_2	105604.73	0.95
	O^- (1s) in LCO@SnO_2	100171.00	
	O^{2-} (1s) in SnO_2	112276.32	0.90
	O^- (1s) in SnO_2	101553.77	
R.T	O^{2-} (1s) in LSCM@SnO_2	93706.99	0.92
	O^- (1s) in LSCM@SnO_2	85741.99	
	O^{2-} (1s) in LCO@SnO_2	101538.60	0.70
	O^- (1s) in LCO@SnO_2	71077.02	
	O^{2-} (1s) in SnO_2	131451.08	0.73
	O^- (1s) in SnO_2	96192.19	

interface of SnO_2 and LCO, resulting in lower baseline resistance of LCO@SnO_2 FITs compared to that of LSCM@SnO_2 FITs. However, LSCM@SnO_2 FITs exhibited dramatically improved resistance variation upon exposure to formaldehyde gas compared with control samples. In case of LSCM@SnO_2 NFs, LSCM particles were immobilized inside NFs, thus the catalytic effect of LSCM particles was less evident, resulting in a small decrease in resistance.

To further demonstrate the catalytic activity of LSCM particles on formaldehyde sensing characteristics, we carried out ex-situ XPS analysis of pristine SnO_2 NTs, LCO@SnO_2 FITs, and LSCM@SnO_2 FITs right after heating the samples at 400 °Cin ambient condition for 5 h. Since the chemisorbed oxygen (O^- and O_2^-) are the main reaction sites for analytes, we specifically investigated the XPS spectra of O 1s. Typically, chemisorbed oxygen species on the surface of SMOs are mainly O^- ions in the temperature range of 200–400 °C.[35] Therefore, we calculated the relative peak area ratio of chemisorbed oxygen to lattice oxygen, *i.e.*, O^-/O^{2-}, which indicates the relative amount of the chemisorbed oxygen on the surface. At first, the O 1*s* spectra of LSCM@SnO_2 FITs, LCO@SnO_2 FITs, and pristine SnO_2 NTs were evaluated at room temperature (Fig. 6c). The peak ratios for LSCM@SnO_2 FITs, LCO@SnO_2 FITs, and pristine SnO_2 NTs were 0.92, 0.70, and 0.73, respectively, which were calculated from peak area values presented in **Table 1**. It was observed that the three peak ratios increased to 1.48, 0.95, and 0.90, respectively (Fig. 6d) after heating at 400 °C for 5 h. In addition, peak areas of O^- were increased for all samples after heating (Table 1), indicating that the main oxygen species on the SMOs at 400 °C are chemisorbed oxygen species. Notably, LSCM@SnO_2 FITs exhibited the highest increase in the peak ratio (60.9%) upon heating, compared to that of LCO@SnO_2 FITs (35.7%) and pristine SnO_2 NTs (23.3%), indicating the increase of the reaction sites for target gas on the surface of SMOs at 400 °C. This result reveals that the surface oxygen sources mainly originated from LSCM particles at an optimized sensing temperature (400 °C). It is well known that the partial substitution of A-site trivalent cation into divalent cation can induce oxygen vacancies for charge compensation.[36] Thus, one can expect the increase in the concentration of surface oxygen species (O^-) by introducing Sr^{2+} at the site of La^{3+}, since oxygen species (O^-) on the surface of perovskite are mainly adsorbed weakly in oxygen vacancies.[20] In addition, electron migration due to formation of heterojunction between SnO_2 and LSCM may reduce Mn^{4+} to Mn^{3+}, resulting in formation of oxygen vacancies for charge compensation. The valences of Mn (Mn^{3+} and Mn^{4+}) in LSCM@SnO_2 FITs compared to single valence of Mn^{4+} in pristine LSCM revealed the partial reduction of Mn^{4+} to Mn^{3+} (Fig. 4f and Fig. S9a). In fact, owing to the chemical nature of Cr that strongly prefers six-fold coordination, it is hard to generate oxygen vacancies in $LaCrO_3$.[37] Fig. S10 proves the effect of substitution, showing the higher surface oxygen ratio for LSCM (1.60) that LCO (1.40) and O^- peak area. Furthermore, the surface oxygen on the perovskite oxides can spread over to the surface of SMOs, similar to the chemical sensitization of noble metal catalysts, *i.e.*, spillover effect.[32] Therefore, LSCM particles provide numerous oxygen species to the surface of SnO_2, leading to the increase in gas reaction sites. As additional LSCM@SnO_2 FITs toward lower binding energy after heating at 400 °C (Fig. S9b). This result was attributed to the increased evidence, we confirmed a slight peak shift of 3*d* peaks of Sn^{4+} of chemisorbed oxygen species on the surface of SnO_2 FITs, which act as surface trap sites, forming upward band bending at the surface.[38] In addition, as shown in Fig. S11, the resistance of LSCM particles was almost constant upon exposure to formaldehyde, indicating that chemical reaction was mainly occurred on the surface of SnO_2 FITs as well as the reaction between LSCM particles and formaldehyde was negligible. Since formaldehyde is a reducing gas, it reacts with the surface oxygen species, donating the trapped electrons back to the conduction band of SMOs by the following equations:[39, 40]

$$HCHO_{(gas)} + 2O^-_{(ads)} \rightarrow CO_{2(gas)} + H_2O_{(gas)} + 2e^-$$

$$HCHO_{(gas)} + O^-_{(ads)} \rightarrow CHOOH_{(gas)} + e^-.$$

Accordingly, peak ratios of chemisorbed oxygen species in LSCM@SnO_2 FITs, LCO@SnO_2 FITs, and pristine SnO_2 NTs (1.48,

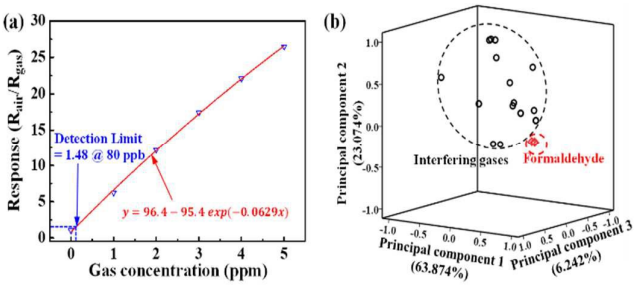

Fig. 7 a) Approximation of detection limit of LSCM@SnO_2 FITs using a calibration curve. b) Pattern recognition based on principal component analysis (PCA) using two sensor arrays (SnO_2 NTs and LSCM@SnO_2 FITs).

View Article Online
DOI: 10.1039/C8TA02725K

Table 2. Recent publications about SMOs-based gas sensors for detecting formaldehyde gas molecules.

Sensing Material	Response (R_{air}/R_{gas})	Detection limit	Operating temperature	Response time	Ref.
Ag@$LaFeO_3$ nanofibers	4.80 at 5 ppm	5 ppm	230 °C	2 s at 20 ppm	[42]
CuO@TiO_2 nanofibers	15.5 at 50 ppm	5 ppm	200 °C	1.4 s at 10 ppm	[43]
WO_3@In_2O_3 nanosheets	25 at 100 ppm	0.1 ppm	170 °C	1 s at 100 ppm	[40]
Hierarchical ZnO architectures	35 at 100 ppm	–	260 °C	1 s at 100 ppm	[44]
Ce@Sn_3O_4 hierarchical microspheres	5.50 at 100 ppm	–	200 °C	4 s at 200 ppm	[45]
SnO_2 microspheres	38.28 at 100 ppm	–	200 °C	17 s at 100 ppm	[46]
Co-rich $ZnCo_2O_4$ Hollow nanospheres	7.5 at 1 ppm	13 ppb	230 °C	149 s at 1 ppm	[47]
LSCM@SnO_2 FITs	26.5 at 5 ppm	80 ppb	400 °C	32 s at 1 ppm	**this work**

0.95, and 0.90, respectively) were directly related to their sensitivity, where LSCM@SnO_2 FITs exhibited exceptional sensitivity toward formaldehyde (R_{air}/R_{gas} = 26.50 @ 5 ppm) compared to that of LCO@SnO_2 FITs (5.17 @ 5 ppm) and SnO_2 NTs (4.85 @ 5 ppm) (Fig. 5a). In short, the catalytic performances of perovskite on the sensing characteristics of SMOs can be maximized by cation substitution. In our case, we introduced Sr and Mn in the site of La and Cr, respectively. As a result, the electron depletion region was increased by doping of Sr, and the amount of surface oxygen species that can be adsorbed on the surface of SMOs was maximized by inducing oxygen vacancies on the perovskite by doping of Sr and Mn.

In addition to the catalytic performance of LSCM particles, the FIT structure has a great influence on the formaldehyde sensing performances. To investigate the structural effect in terms of surface area and porosity, we carried out Brunauer-Emmett-Teller (BET) analysis for surface area and pore size distribution of 5 wt% LSCM@SnO_2 FITs and 5 wt% LSCM@SnO_2 NFs. The LSCM@SnO_2 FITs exhibited larger surface area (10.79 m^2 g^{-1}) compared to that of LSCM@SnO_2 NFs (8.63 m^2 g^{-1}), which is attributed to the tubular structure, *i.e.*, fibers inside the tubes (Fig. 6e). Furthermore, the pore size distribution demonstrated higher pore volume of LSCM@SnO_2 FITs in the mesopore range (2–50 nm) compared to LSCM@SnO_2 NFs, which implies that hollow structures of LSCM@SnO_2 FITs (Fig. 6f) facilitate gas permeation. Due to enlarged surface area and high porosity, LSCM@SnO_2 FITs showed higher response (26.50 to 5 ppm) and shorter response time (<32s) toward formaldehyde gas than LSCM@SnO_2 NFs (6.15 to 5 ppm and response time of <32s) (Fig. 5a and b.) These results demonstrated the synergistic effect between FIT structures and LSCM particles, and the significance of FITs for effective catalytic performance of perovskite oxides.

To demonstrate the potential capability of LSCM@SnO_2 FITs for practical application in real-time monitoring of formaldehyde gas, a limit of detection of LSCM@SnO_2 FITs sensors was approximated by extrapolating the sensing results (Fig. 7a). The calibrated curve anticipated a response of 1.48 to 80 ppb of formaldehyde. Considering that WHO (World Health Organization) indoor guideline level of formaldehyde is 80 ppb,[41] this result implies the potential feasibility of LSCM@SnO_2 FITs for practical implementation as CH_2O detecting sensors. In addition, to confirm the feasibility of LSCM@SnO_2 FITs for the selective detection of formaldehyde against interfering gases, a principal component analysis (PCA) was conducted using two different sensors, *i.e.*, pristine SnO_2 NTs and 5 wt% LSCM@SnO_2 FITs (Fig. 7b). PCA is a statistical tool that can classify sensing data based on their similarity. The formaldehyde molecules were clearly distinguished in a three-dimensional space from interfering gases (H_2S, C_7H_8, NH_3, C_2H_6O, C_8H_{10}, CO, and C_5H_{12}), showing superior selectivity of the sensor array. The sensing performance of the rationally designed LSCM@SnO_2 FITs, exhibited the highest ranking formaldehyde sensing characteristics in terms of sensitivity, response time, and detection limit, in comparison with reported SMOs-based formaldehyde gas sensors (**Table 2**).[40, 42-47] The selective detection capability of LSCM@SnO_2 FITs toward formaldehyde signifies that it can be potentially applied to real-time monitoring of indoor air quality.

Conclusion

In summary, we successfully utilized perovskite $La_{0.75}Sr_{0.25}Cr_{0.5}Mn_{0.5}O_{3-\delta}$ (LSCM) particles as new catalysts for electrospun 1D SMOs-based chemiresistive materials. The LSCM particles were tightly immobilized in the nanotubular structures upon calcination at fast ramping rate. During calcination, the LSCM particles impeded the migration of Sn ions as well as the outward diffusion of gaseous byproducts, thereby forming fibrous structure inside nanotubes, *i.e.*, LSCM@SnO_2 FITs. Interestingly, LSCM particles affected the formaldehyde sensing performances of SnO_2 in terms of catalytic and structural effects, *i.e.*, i) the oxygen providing effect of LSCM perovskite, which serves as a role of chemical sensitization like noble metal catalysts, ii) large heterojunction effect due to differences in work function (4.55 eV of SnO_2 versus 6.8 eV of LSCM), resulting in larger electron depletion region, and iii) structural effect of FIT structures with enlarged surface area and high porosity. On the basis of these advantages, LSCM@SnO_2 FITs showed superior response

View Article Online
DOI: 10.1039/C8TA02725K

toward 5 ppm of formaldehyde (R_{air}/R_{gas} = 26.50 @ 400 °C), with high selectivity and stability. Based on these results, chemiresistors using LSCM@SnO_2 FITs as sensing layers can find application in real-time monitoring of indoor air quality. Furthermore, a combination of perovskite oxides and nanostructured SMOs can be applied as chemical gas sensors, providing excellent catalytic effects.

Acknowledgements

This work was supported by the National Research Foundation of Korea (NRF), grant no. 2014R1A4A1003712 (BRL Program). This research also was supported by Research and Business Development Program through the Korea Institute for Advancement of Technology (KIAT) funded by the Ministry of Trade, Industry and Energy (MOTIE) (grant number: N0002418). This work was also supported by Wearable Platform Materials Technology Center (WMC) funded by National Research Foundation of Korea (NRF) Grant of the Korean Government (MSIP) (No. 2016R1A5A1009926).

Notes and references

1 R. Kostiainen, *Atmo. Environ.*, 1995, **29**, 693-702.
2 P. Wargocki, D. P. Wyon, Y. K. Baik, G. Clausen and P. O. Fanger, *Indoor air*, 1999, **9**, 165-179.
3 A. Saito, H. Tanaka, H. Usuda, T. Shibata, S. Higashi, H. Yamashita, N. Inagaki and H. Nagai, *Environ. Toxicol.*, 2011, **26**, 224-232.
4 X. Tang, Y. Bai, A. Duong, M. T. Smith, L. Li and L. Zhang, *Environ. Int.*, 2009, **35**, 1210-1224.
5 T. Salthammer, S. Mentese and R. Marutzky, *Chem. Rev.*, 2010, **110**, 2536-2572.
6 S.-J. Choi, I. Lee, B.-H. Jang, D.-Y. Youn, W.-H. Ryu, C. O. Park and I.-D. Kim, *Anal. Chem.*, 2013, **85**, 1792-1796.
7 H.-J. Kim and J.-H. Lee, *Sens. Actuators B*, 2014, **192**, 607-627.
8 S.-J. Kim, S.-J. Choi, J.-S. Jang, N.-H. Kim, M. Hakim, H. L. Tuller and I.-D. Kim, *ACS Nano*, 2016, **10**, 5891-5899.
9 S.-J. Choi, B.-H. Jang, S.-J. Lee, B. K. Min, A. Rothschild and I.-D. Kim, *ACS Appl. Mater. Interfaces*, 2014, **6**, 2588-2597.
10 J. S. Jang, S. J. Choi, S. J. Kim, M. Hakim and I. D. Kim, *Adv. Funct. Mater.,* 2016, **26**, 4740-4748.
11 Y. J. Hong, J. W. Yoon, J. H. Lee and Y. C. Kang, *Chem. Eur. J.*, 2015, **21**, 371-376.
12 H.-G. Wang, Y.-H. Li, W.-q. Liu, Y.-C. Wan, Y.-W. Li and Q. Duan, *RSC Adv.*, 2014, **4**, 23125-23130.
13 W.-T. Koo, S.-J. Choi, S.-J. Kim, J.-S. Jang, H. L. Tuller and I.-D. Kim, *J. Am. Chem. Soc.*, 2016, **138**, 13431-13437.
14 F. Maillard, S. Schreier, M. Hanzlik, E. Savinova, S. Weinkauf and U. Stimming, *Phys. Chem. Chem. Phys.,* 2005, **7**, 385-393.
15 S. Tao, J. T. Irvine and J. A. Kilner, *Adv. Mater.*, 2005, **17**, 1734-1737.
16 C. Jin, X. Cao, L. Zhang, C. Zhang and R. Yang, *J. Power Sources*, 2013, **241**, 225-230.
17 T. Seiyama, *Catal. Rev.*, 1992, **34**, 281-300.
18 S. Royer, D. Duprez, F. Can, X. Courtois, C. Batiot-Dupeyrat, S. Laassiri and H. Alamdari, *Chem. Rev.*, 2014, **114**, 10292-10368.
19 H. Zhu, P. Zhang and S. Dai, *ACS Catal.*, 2015, **5**, 6370-6385.
20 J. Zhu, H. Li, L. Zhong, P. Xiao, X. Xu, X. Yang, Z. Zhao and J. Li, *ACS Catal.*, 2014, **4**, 2917-2940.
21 I.-D. Kim, A. Rothschild and H. L. Tuller, *Acta Mater.*, 2013, **61**, 974-1000.
22 H.-J. Lin, J. P. Baltrus, H. Gao, Y. Ding, C.-Y. Nam, P. Ohodnicki and P.-X. Gao, *ACS Appl. Mater. Interfaces*, 2016, **8**, 8880-8887.
23 V. R. Channu, R. Holze, E. H. Walker and R. R. Kalluru, *New J. Glass Ceram.*, 2011, **1**, 112-115.
24 J. Wu, D. Zeng, X. Wang, L. Zeng, Q. Huang, G. Tang and C. Xie, *Langmuir*, 2014, **30**, 11183-11189.
25 H. Hayashi, M. Watanabe and H. Inaba, *Thermochim. Acta*, 2000, **359**, 77-85.
26 D. Bao, P. Gao, X. Zhu, S. Sun, Y. Wang, X. Li, Y. Chen, H. Zhou, Y. Wang and P. Yang, *Chem. Eur. J.*, 2015, **21**, 12728-12734.
27 A. Nashim and K. Parida, *J. Mater. Chem. A*, 2014, **2**, 18405-18412.
28 Z. Dai, C.-S. Lee, B.-Y. Kim, C.-H. Kwak, J.-W. Yoon, H.-M. Jeong and J.-H. Lee, *ACS Appl. Mater. Interfaces*, 2014, **6**, 16217-16226.
29 M. Ardigo, A. Perron, L. Combemale, O. Heintz, G. Caboche and S. Chevalier, *J. Power Sources*, 2011, **196**, 2037-2045.
30 H. Nesbitt and D. Banerjee, *Am. Mineral.*, 1998, **83**, 305-315.
31 J.-S. Jang, W.-T. Koo, S.-J. Choi and I.-D. Kim, *J. Am. Chem. Soc.*, 2017, **139**, 11868-11876.
32 I.-S. Hwang, J.-K. Choi, H.-S. Woo, S.-J. Kim, S.-Y. Jung, T.-Y. Seong, I.-D. Kim and J.-H. Lee, *ACS Appl. Mater. Interfaces*, 2011, **3**, 3140-3145.
33 S.-J. Kim, S.-J. Choi, J.-S. Jang, H.-J. Cho and I.-D. Kim, *Acc. Chem. Res.*, 2017, **50**, 1587-1596.
34 R. Jacobs, J. Booske and D. Morgan, *Adv. Funct. Mater.*, 2016, **26**, 5471-5482.
35 M. E. Franke, T. J. Koplin and U. Simon, *Small*, 2006, **2**, 36-50.
36 D. L. Chen, K. L. Pan and M. B. Chang, *J. Environ. Sci.*, 2016, **56**, 131-139.
37 S. Tao and J. T. Irvine, *Nat. Mater.*, 2003, **2**, 320-323.
38 R. Cavicchi, M. Tarlov and S. Semancik, *J. Vac. Sci. Technol. A*, 1990, **8**, 2347-2352.
39 H. Du, J. Wang, M. Su, P. Yao, Y. Zheng and N. Yu, *Sens. Actuators B*, 2012, **166**, 746-752.
40 Y. Cao, X. Zou, Y. He and G.-D. Li, *Sens. Actuators B*, 2017, **252**, 232-238.
41 T. Salthammer, *Int. J. Hyg. Environ. Health*, 2015, **218**, 433-436.
42 W. Wei, S. Guo, C. Chen, L. Sun, Y. Chen, W. Guo and S. Ruan, *J. Alloys Compd*, 2017, **695**, 1122-1127
43 J. Deng, L. Wang, Z. Lou and T. Zhang, *J. Mater. Chem. A*, 2014, **2**, 9030-9034.
44 J. Cao, S. Wang and H. Zhang, *Mater. Lett.*, 2017, **202**, 44-47.
45 X. Ma, J. Shen, D. Hu, L. Sun, Y. Chen, M. Liu, C. Li and S. Ruan, *J. Alloys Compd*, 2017, **726**, 1092-1100.
46 Y. Li, N. Chen, D. Deng, X. Xing, X. Xiao and Y. Wang, *Sens. Actuators B*, 2017, **238**, 264-273.
47 H. J. Park, J. Kim, N.-J. Choi, H. Song and D.-S. Lee, *ACS Appl. Mater. Interfaces*, 2016, **8**, 3233-3240.

View Article Online
DOI: 10.1039/C8TA02725K

The table of contents